Journal of Applied Fluid Mechanics, Vol. 16, No. 10, pp. 1938-1950, 2023.
Available online at www.jafmonline.net, ISSN 1735-3572, EISSN 1735-3645.
https://doi.org/10.47176/jafm.16.10.1863

Experimental and Simulation Study on the Emissions of a Multi-Point Lean Direct Injection Combustor

P. Zhu, Q. Li, X. Feng, H. Liang†, J. Suo and Z. Liu

School of Power and Energy, Northwestern Polytechnical University, Xi`an, Shaanxi, 710072, China

†*Corresponding Author Email: hx_liang@nwpu.edu.cn*

ABSTRACT

Spurred by the world's attention to pollution emissions from commercial aero-engines, the International Civil Aviation Organization (ICAO) has made more stringent emission regulations for civil aircraft engines, especially the NOx emission.This paper develops a Five-Point lean direct injection (LDI) combustor with three swirler schemes to reduce the emissions of commercial aircraft engines. The flowfield of the combustor is studied numerically. Moreover, the combustion efficiency and gaseous emissions in different inlet conditions and fuel ratios of the main stage (α) are studied experimentally. The corresponding results reveal that, under a fuel-air ratio (FAR) between 0.0130 and 0.0283 and an α value between 30% and 60%, the combustion efficiency is 99.18%, 98.83%, and 99.03% when the pilot stage works alone, and 99.69%, 99.23%, and 99.75% when the pilot and main stage work simultaneously. Furthermore, the experimental results suggest that the NOx emission decreases as α increases, demonstrating that the convergent swirler has a tremendous advantage in reducing NOx emissions over Venturi.

Article History

Received March 13, 2023
Revised May 10, 2023
Accepted May 19, 2023
Available online July 29, 2023

Keywords:

LDI technology
NOx emissions
Combustion performance
Combustor
Venturi

1. INTRODUCTION

Spurred by the world's attention to pollution emissions from commercial aero-engines, the International Civil Aviation Organization (ICAO) has made more stringent emission regulations for civil aircraft engines, especially the NOx emission (Lieuwen & Yang 2013; Zhu et al., 2021). Therefore, modern civil aircraft engines have developed towards reducing their emissions, and to date, three main low-emission combustion concepts have been proposed: Rich-burn Quick-quenching Lean-burn (RQL) (Mckinney et al., 2007; Chen et al., 2019), Lean Premixed Prevaporized (LPP) (Foust et al., 2013; Mongia 2013; Wang et al., 2016), and Lean Direct Injection (LDI) (Tacina & Wey, 2008; Heath et al., 2014, 2016). RQL technology has a quick-quenching process with the stoichiometry ratio conditions coming up, producing many NOx emissions. Thus, RQL technology has the limited potential to reduce emissions. However, lean burn technology does not suffer from this problem and has tremendous potential to reduce emissions. The LPP and LDI technology are typical concepts of lean burn combustion (Kyprianidis & Dahlquist 2017).

Although the LPP technology has a low emission level with a practical design and development, it suffers from several inescapable problems (e.g., auto ignition, flashback, and combustion instability) due to the premixed and pre-vaporized processes (Lieuwen et al., 2001; Hatem et al., 2018). Furthermore, combustion instability has been the most prominent restriction for developing LPP technology. Unlike LPP, LDI fuel and air are directly injected into the combustor without premixing and pre-vaporizing. So, the autoignition and flashback will occur in the combustor, making the combustion instability less severe than LPP. Also, LDI and LPP are equally capable of reducing emissions. Therefore, LDI technology has become an effective way of reducing pollution. Many studies on LDI technology have been conducted, such as the flow field (Fan et al., 2020; Huang et al. 2020; Tian et al. 2022; Xi et al. 2022), the NOx emission (Gugulothu & Nutakki, 2019; Zargar, 2020; Raju & Wey 2020; Xu et al., 2021), the spray characteristics (Wang et al., 2021), and the ignition performance (Wang et al., 2020).

The key to the LDI technology is ensuring the perfect fuel atomization and a uniform mixture with air. Then, the lean combustible mixture is formed at the combustor's dome, reducing the NOx emission by reducing the temperature of the combustion zone (Fu, 2008). Furthermore, the large-flow nozzle has been substituted

NOMENCLATURE

FAR	the fuel-air ratio of the combustor	*EINOx*	emission index of NOx
FARBAL	the balance of the fuel-air ratio	m_{air}	total air massflow
$FAR_{emissions}$	the calculation value of the fuel-air ratio	$m_{\mathrm{air,main}}$	air mass flow of the main stage
$FAR_{facility}$	the ratio of metered fuel and air mass flow rates	$m_{\mathrm{air,pilot}}$	air mass flow of the pilot stage
FAR_{stoi}	stoichiometry of kerosene	m_{f}	total fuel massflow
RQL	Rich-burn Quick-quenching Lean-burn	$m_{\mathrm{f,main}}$	fuel mass flow of the main stage
LPP	Lean Premixed Prevaporized	$m_{\mathrm{f,pilot}}$	fuel mass flow of the main stage
LDI	Lean Direct Injection	P_3	burner inlet pressure (BIP)
EICO	emission index of CO	T_3	burner inlet temperature (BIT)
EIUHC	emission index of UHC	T_4	burner outlet temperature
α	fuel ratio of the main stage	Φ_{dome}	local equivalence ratio of the dome
Φ_{main}	local equivalence ratio of the main stage	Φ_{pilot}	local equivalence ratio of the pilot stage

from multiple small-flow nozzles to achieve the above objectives. This concept is referred to as Multi-Point Lean Direct Injection (MPLDI), which is one of the significant directions of low-pollution combustion technology. Many scholars have conducted research on the MPLDI concept science 1990s, with the most representative being the three generations of the Swirl-Venturi Lean Direct Injection (SV-LDI) proposed by NASA (National Aeronautics and Space Administration).

Many studies have been carried upon the flow field (Davoudzadeh, 2004; Fu, 2008; Chiming et al., 2007; Villalva, 2013; Tedder et al., 2014), the emissions (Cai, 2006; Patel et al., 2007, Patel & Menon, 2008; Hicks et al., 2012; Dewanji et al., 2012; Hicks & Tacina 2013; Dewanji & Rao, 2015a,b), and the combustion instability (Gejji et al., 2014; Huang et al., 2014). These studies reveal that the MPLDI concept can reduce NOx emissions effectively. Indeed, the NOx emissions of the three SV-LDI generations, SV-LDI- Ⅰ (Tacina et al., 2016), SV-LDI- Ⅱ (Huang et al., 2014), and SV-LDI- Ⅲ (ISABE, 2017) are reduced by 60%, 75%, and 85% compared with CAPE 6. Although the MPLDI concept has proven considerable potential in reducing NOx emission, it is still difficult to apply in engines, and therefore research on the performance of the MPLDI combustion chamber is still of great significance.

This paper considers a Five-Point LDI combustor to verify the possibility of MPLDI application on aircraft engines. This combustor is designed according to a particular aircraft engine's landing take-off cycle parameter. Moreover, three different schemes are studied to find the optimal plan.

2. FIVE-POINT LDI COMBUSTOR

This paper proposes a Five-Point LDI Combustor. To reduce the NOx emission, the combustion air is 65% of the total air in the combustor. Therefore, the combustion zone temperature can be reduced. The remaining air is used for liner cooling and induction holes. The tangential air inlet has already been used in the liner cooling holes and has proven its efficient cooling capability (Yu et al., 2016).

Figure 1 illustrates a dome comprising five similar little swirler modules. The dome of the combustor

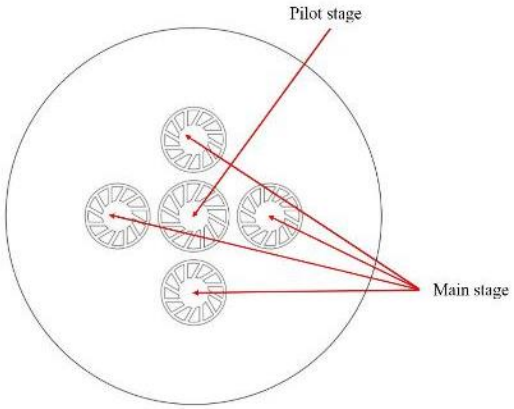

Fig. 1 Dome of the five-point LDI combustor

concludes the pilot and main stages, with the fuel of each stage being independently controlled. The swirler module at the center of the dome is the pilot stage, and the rest four modules around the pilot stage comprise the main stage. The pilot stage operates independently, having a rich equivalent ratio to form the flame stability at low conditions. The pilot and the main stages work together at high conditions with a low equivalent ratio to reduce NOx emission.

Figure 2 depicts the combustor's flow characteristics, with the flow field at the central section including three typical vertex structures: the center recirculation zone, the recirculation zone of the main stage, and the corner recirculation zone. At low conditions, the center recirculation zone plays a significant role in flame stability.

There are two swirler modules presented in Fig.3. One is the same as the SV-LDI dome, comprising an axial swirler with a Venturi exit and a pressure-swirling nozzle located in the throat of the Venture exit. The other module comprises an axial swirler with a convergent exit and a nozzle at the export of the convergent exit. Without the exit, the details of the swirler module are identical. Moreover, the radial interval between the axial and tangential velocity peaks, and the recirculation flow rate is increased due to the Venturi exit (Fristrom & Westenberg 1965). The pilot swirlers with five-point LDI were mainly responsible for stabilizing flames under low operating conditions, hence the choice of 40° blade angle for better

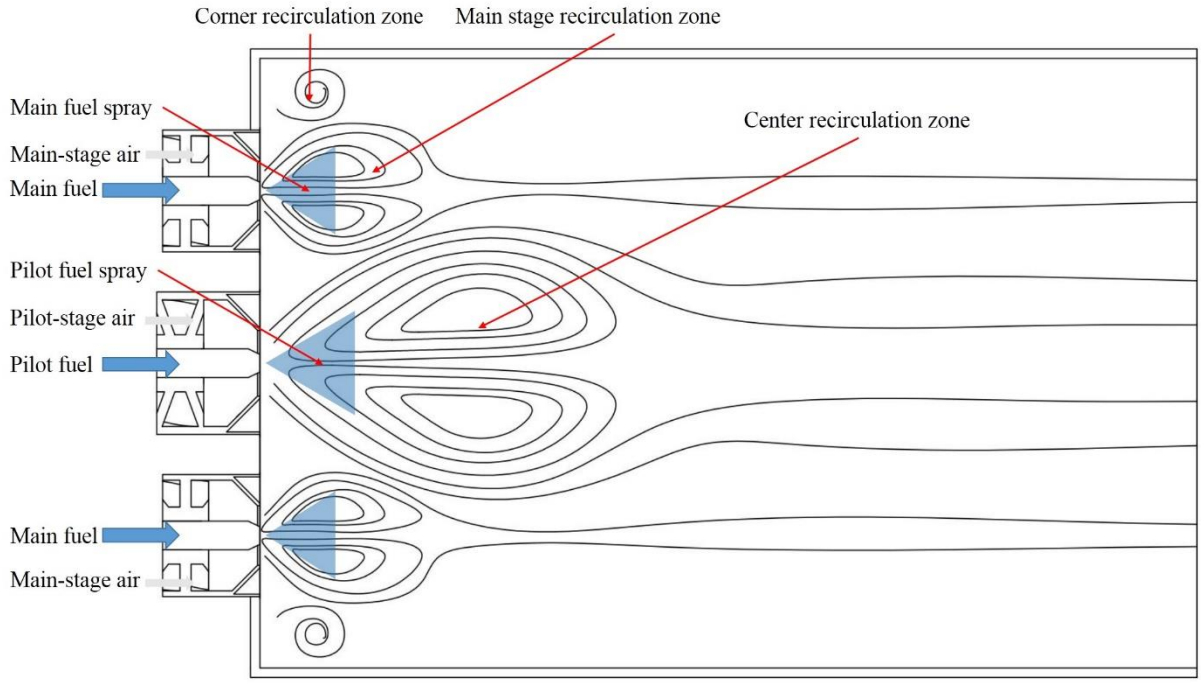

Fig. 2 Scheme of the five-point LDI combustor

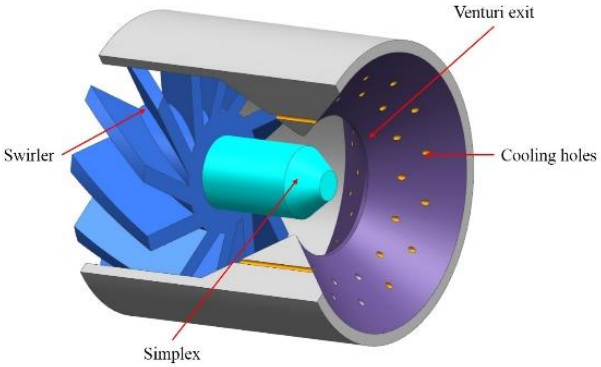

(a) Venturi swirler module

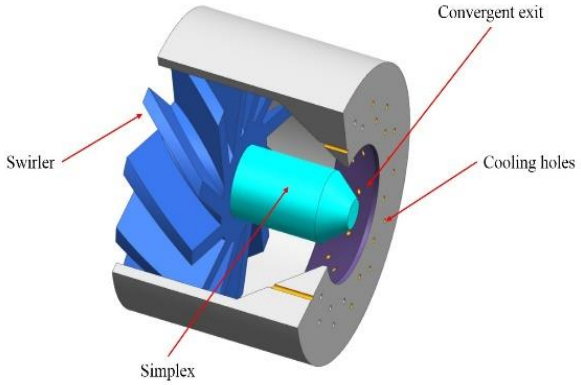

(b) Convergent swirler module

Fig. 3 Scheme of two different swirler modules

flame stability under low operating conditions. As for the main swirlers, the goal was to reduce pollutant emissions from the combustor. Therefore, the blade angle of 32° was chosen to reduce pollutant emissions under high operating conditions. This paper obtains the best combustion performance by studying three dome programs, with Table 1 presenting their basic structural parameters.

Table 1 Parameter setup for the three cases

Parameter	Case A	Case B	Case C
Pilot swirl angle	40°	40°	40°
Structure of the pilot stage	Venturi	Convergent	Venturi
Main swirl angle	32°	32°	32°
Structure of the main stage	Venturi	Convergent	Convergent

To facilitate the dome's processing, the swirler blades employed are straight, and the swirl angle is the deflection angle between the vanes and the incoming flow direction. In this paper, considering the flame's stability when the pilot stage operates alone and the requirement reducing the pollution emissions when the pilot and the main stages work together, we set the swirler blade angle of the pilot stage at 40°and the main stage is 32°.

It should be noted that the nozzles of the pilot and main stages are pressure atomized, the spray has a solid cone mode, and the spray cone angle is 90°.

3. EXPERIMENTAL SETUP

3.1 Test Rig

Figure 4 illustrates the single-tube combustor test rig, which contains the inlet, combustion, and measurement sections. The inlet section measures the test rig's inlet temperature (BIT) and inlet total pressure (BIP) and introduces the fuel for both the pilot and the main stages. The inlet temperature is arranged at 50mm, and the inlet pressure is arranged at 150mm from the head of the combustion chamber.

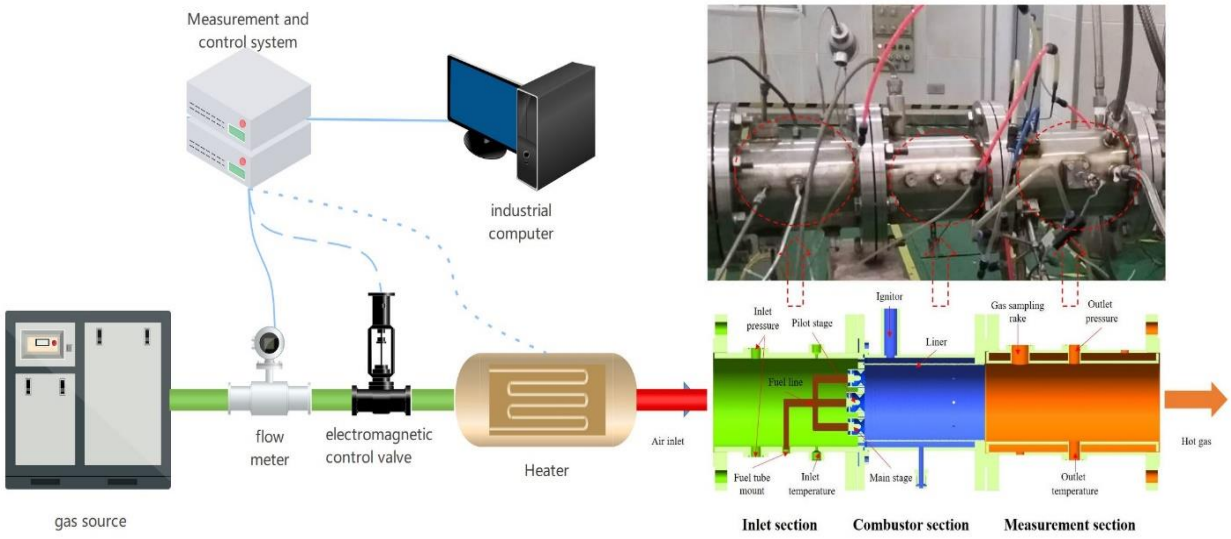

Fig. 4 Test rig of the single-tube combustor

The combustion section, which completed the intense physical and chemical reaction process, is the core of this experimental research, containing the LDI dome, casing, igniter, and liner. The igniter is located on the casing, and seven K-type thermocouples are on the liner to monitor the wall temperature. The liner is where the combustion reaction occurs, with a length of 280mm and a diameter of 110mm.

The measurement section mainly realizes the outlet temperature and total pressure measurement, with the corresponding measurement points arranged at 130mm from the combustion chamber's outlet. A 7-point water-cooled gas sampling probe was arranged 55mm downstream of the combustor outlet to ensure the consistency of the gas sampling composition with the combustion chamber.

The inlet air mass flow is measured by the Rosemount orifice flow meter (accuracy of ±1%), and the fuel mass flow rate is measured using the Kracht gear flow meter (accuracy of ±0.3%). The inlet and outlet temperatures are measured using the K-type and S-type thermocouples (accuracy of ±0.25%). Finally, the inlet and outlet pressure are measured using the Rosemount pressure transducer (accuracy of ±0.5%). The fuel is aviation kerosene in all the tests.

3.2 Test Conditions

For those formatting by hand, section and subsection headings are numbered using Arabic numerals separated by '.' Sections (heading 1, in Word) are 11 pt, boldface, and flush left. They are hanging 0.63 cm (0.25 inches) and are typed with small caps font effect. Subsections (heading 2, in Word) are 10 pt, boldface, and flush left. Further sub-subsections (heading 3, in Word) are 10 pt, boldface, and flush left. All levels below this are unnumbered, 10pt, boldface, with text beginning immediately following the heading on the same line.

The fuel-air ratio (FAR) of the combustor is defined as follows:

$$\mathrm{FAR} = \frac{m_{\mathrm{f}}}{m_{\mathrm{air}}} \tag{1}$$

Table 2 Test conditions

Parameter	Unit	Range
T3	K	449-700
P3	MPa	0.3-0.5
FAR	N/A	0.0135-0.0283
α	%	30-60

where mf and mair are the fuel and air mass flow, respectively. The local equivalence ratio of the pilot stage, main stage, and dome are:

$$\phi_{\mathrm{pilot}} = \frac{(m_{\mathrm{f,pilot}}/(m_{\mathrm{air,pilot}})}{\mathrm{FAR_{stoi}}} \tag{2}$$

$$\phi_{\mathrm{main}} = \frac{(m_{\mathrm{f,main}})/(m_{\mathrm{air,main}})}{\mathrm{FAR_{stoi}}} \tag{3}$$

$$\phi_{\mathrm{dome}} = \frac{(m_{\mathrm{f,pilot}}+m_{\mathrm{f,main}})/(m_{\mathrm{air,dome}})}{\mathrm{FAR_{stoi}}} \tag{4}$$

where mf,pilot and mf,main are the fuel mass flow of the pilot and main stage, respectively, mair,pilot, mair,main, and mair,dome are air mass flow of the pilot, main stage, and dome, and FARstoi is the stoichiometry ratio of aviation kerosene.

The main stage's fuel ratio (α) is defined as follows:

$$\alpha = \frac{m_{\mathrm{f,main}}}{(m_{\mathrm{f,pilot}}+m_{\mathrm{f,main}})} \times 100\% \tag{5}$$

All experiments are conducted for a certain type of turboprop engine under typical LTO cycle conditions (idle, climb, and take-off). Due to the limited capacity of the test bench, the equal Mach number method is used to simulate the depressurization of the climb and take-off conditions and determine this paper's research conditions, as reported in Table 2.

3.3 Gas Analysis Method and Data Analysis

The test rig is equipped with a standard gas bench to measure the CO, CO2, NOx, and unburned hydrogen,

Table 3 Introduction of gas analyzers

Gas	Model	Principle	Range	Accuracy
CO/CO2	CAI 600	Non-Dispersive Infrared Analyzer (NDIR)	0-500ppm/0-10%	1%
UHC	CAI 600	Flame Ionization Detector (FID)	0-500ppm	1%
NOx	CAI 600	Chemiluminescent Detector (CLD)	0-1000ppm	1%
H2O	Edgetech	Chilled Mirror (CM)	0-20000ppm	1%
O2	CAI 600	Paramagnetic method	0-25%	1%

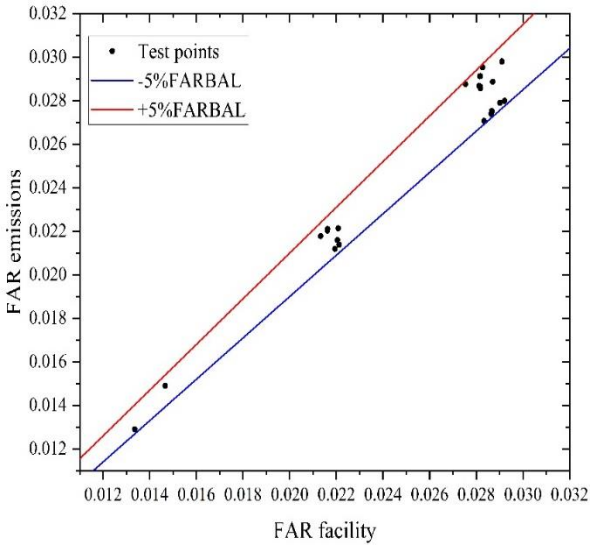

Fig. 5 FARBAL of all the test conditions

carbon so that emissions can be measured according to the ICAO regulations (SAE ARP 1256D (SAE, 2011). The details of the gas analyzers are reported in Table 3, with the gas analysis system comprising a sampling rank pretreatment system, analysis system, and data collection system. The 7-point water-cooled sampling rake employs primary expansion and convection cooling to freeze the chemical reaction effectively. This setup has appealing thermal protection characteristics and pressure-bearing capacity, ensuring a stable operation in the combustion gas. Given that the gas enters the pretreatment system through the transportation pipeline at 165±15℃ by using electric heat, the NOx and UHC condensation can be prevented from affecting the results' accuracy. Then the gas flows in the analysis system, with the UHC analyzer adopting a hydrogen flame ionization detection method, the NOx analyzer adopting the chemiluminescence method, and the CO and CO2 analyzer relying on the non-dispersive infrared analysis principle. When the emission data is obtained from the analyzers, the post-processing stage considers the SAE ARP 1533 (SAE, 2013) regulations.

The fuel-air ratio balance is an important parameter to measure the effectiveness of gas analysis, as it reflects the sampling rake's arrangement rationality. The smaller the relative deviation of the fuel-air ratio, the better the sample gas collected at the sampling rake, representing the average value of the gas component concentration at the combustor outlet. The fuel-air ratio balance is calculated based on (6). Furthermore, the target value is within ±5%. Figure 5 illustrates the FARBAL at all test conditions, highlighting that all results are valuable for the FARBAL and all test conditions are within ±5%.

$$\text{FARBAL} = 100 \times \frac{(\text{FAR}_{\text{emissions}} - \text{FAR}_{\text{facility}})}{\text{FAR}_{\text{facility}}} \tag{6}$$

3.4 Uncertainty Analysis

The uncertainty analysis was conducted to evaluate the data error of data, with the detailed calculation method provided in the SAE ARP 1533 (SAE, 2013) and described in the Appendix.

According to the analysis results, the emission index (EI, grams of emission product per kilogram fuel) uncertainty and efficiency are within ±1.8% and ±0.008%, respectively.

4. SIMULATION METHODOLOGY

4.1 Turbulence Model

We select the realizable k-ε model to solve the combustor's flow field. Additionally, this model can well predict the complex swirls of low and medium strength, such as jet impingement, shear flow, separated flow, and swirling flow, and can well match the calculation of swirl and separated flow in the aero-engine combustion chamber. This model is mainly calculated based on the Boussinesq assumption, which first connects the Reynolds stress with the average velocity gradient, then adds a formula to the eddy viscosity coefficient and a new transport equation to the dissipation rate to determine the eddy viscosity coefficient. The transport equations of the model's turbulent kinetic energy and dissipation rate are as follows:

$$\frac{\partial}{\partial t}(\rho k) + \frac{\partial(\rho k u_i)}{\partial x_i} = \frac{\partial}{\partial x_i}\left[\left(\mu + \frac{\mu_\tau}{\sigma_k}\right)\frac{\partial k}{\partial x_j}\right] + G_k + G_b - \rho\varepsilon - Y_M + S_k \tag{7}$$

$$\frac{\partial}{\partial t}(\rho \varepsilon) + \frac{\partial(\rho k u_i)}{\partial x_i} = \frac{\partial}{\partial x_i}\left[\left(\mu + \frac{\mu_\tau}{\sigma_s}\right)\frac{\partial \varepsilon}{\partial x_j}\right] + \rho C_1 E\varepsilon - \rho C_2 \frac{\varepsilon^2}{k+\sqrt{\nu\varepsilon}} + G_{1s}\frac{\varepsilon}{k}C_{3s}G_b + S_s \tag{8}$$

The eddy viscosity coefficient formula is as follows:

$$\mu_t = \rho C_\mu \frac{k^2}{\varepsilon} \tag{9}$$

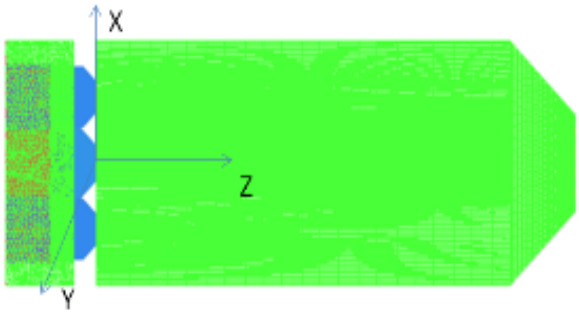

Fig. 6 Grid of multi-point injection combustor

4.2 Combustion Model

The combustion reaction in an aero-engine combustor involves not only a turbulent flow and fuel atomization but also the chemical reaction of the combustible mixture and convection heat transfer of the high-temperature gas. The reaction mechanism is very complex, with this paper's combustor model being a multi-point lean, direct injection model. Thus, the non-premixed PDF model simulates the turbulent combustion process. The PDF transport equation model solves the conservation equation of the component probability density function, which simulates a turbulent flow and chemical interaction combustion process by considering a detailed chemical reaction mechanism with high calculation accuracy and reliable results. Therefore, the PDF transport equation is suitable for non-premixed, fully premixed, and partially premixed combustion. The non-premixed PDF model assumes that the diffusivity of each reaction component is the same. So the component equation can be simplified into a single mixed combination of equations, and the concentration of each component can be derived by solving this equation set. The average mixing fraction equation is as follows, which has been widely used to simulate turbulent diffusion flames:

$$\frac{\partial}{\partial t}\left(\rho\bar{f}\right)+\nabla\left(\rho\bar{v}\bar{f}\right)=\nabla\left(\frac{\mu_t}{\sigma_t}\nabla\bar{f}+S_m+S_{user}\right) \qquad (10)$$

where S_m is the mass of liquid droplets or reaction particles of liquid fuel transferred into the gas phase, and S_{user} is a user-defined source item, $\bar{f}$ is the mixture fraction,v is the velocity.

4.3 Gridding

This paper combines the hexahedron and tetrahedron grids to divide the single-tube combustor grids. At the same time, to ensure good grid quality, the grid of the hydrocyclone part is locally densified to improve the calculation accuracy. The grid division is illustrated in Fig. 6.

The boundary conditions of the calculation model are the same as the test conditions, and the turbulence control equation is k- ε. Moreover, the combustion model is the PDF transport equation model, the second-order accurate discrete format discretizes the control equation, the second-order upwind format discretizes the convection term, the pressure velocity coupling algorithm is SIMPLE, and the fuel nozzle is the atomizing pressure nozzle.

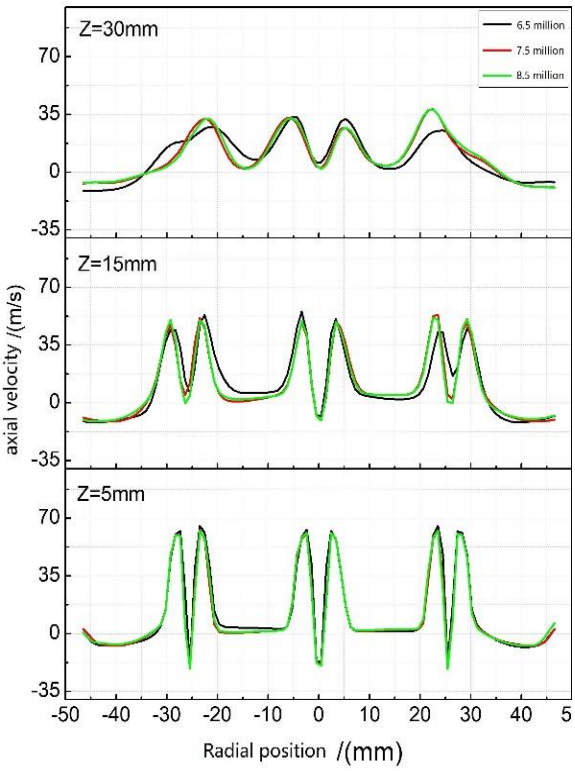

Fig. 7 Distribution of the combustor's axial velocity along the radial position

4.4 Grid independence Verification

To eliminate the impact of grid division on the calculations, this section conducts grid independence verification.

Three calculation grids for the single tube combustor model, 6.5 million, 7.5 million, and 8.5 million, from sparse to dense, are established. The same boundary conditions and turbulence model are used for the calculations, and at the same time, the weighted average axial velocity of the mass flow at the cross section at Z=30 mm is monitored. When the calculation residual is less than 10-4, and the relative fluctuation of the monitored axial velocity is less than 1% and remains more than 150 steps, the numerical calculation can be considered convergent and stable.

The calculation results are illustrated in Fig. 7. In this paper, the axial velocity distribution curves along the radial direction at the combustor head outlet Z=5mm, Z=15mm, and Z=30mm are selected, respectively, which represent the velocity distribution at the cyclone outlet and the velocity distribution in the core recirculation zone.

Figure 7 reveals that at the combustor head outlet Z=5mm, the combustor's axial velocity distribution curve for the three calculation grids is the same. However, at the axial positions Z=15mm and Z=30mm, the axial velocity combustor's distribution curve for the 6.5 million calculation grids differs from the 7.5 million and 8.5 million. The velocity distribution curves of 7.5 million and 8.5 million are the same. Therefore, the subsequent grid is divided into 7.5 million computational grids.

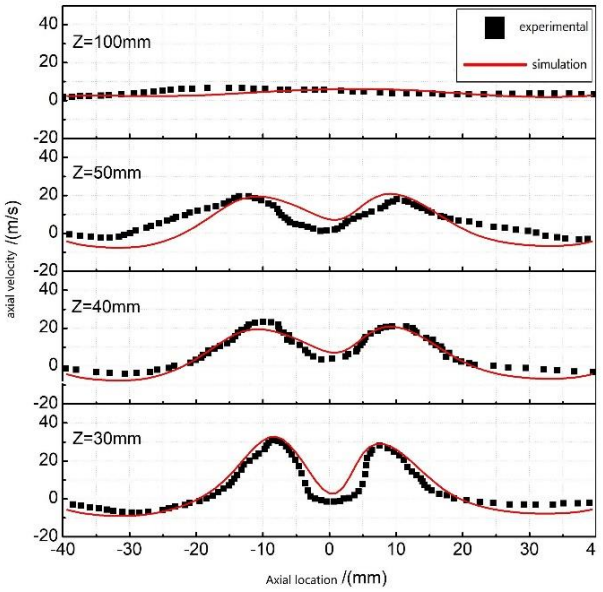

Fig. 8 Comparison curve of the axial velocity distribution along the radial direction at different axial positions

4.5 Verification of the Calculation Model

The PIV experimental results are used to verify the numerical simulation method used in this paper. Figure 8 compares the numerical simulation and experimental results of the axial velocity at different axial positions, revealing that the axial velocity and radial distribution curves are the same. Therefore, the proposed numerical simulation method can predict the flow field in the combustion chamber.

5. RESULTS AND DISCUSSION

5.1 Flow Characteristics of the Combustor

This paper employs the Realizable k-ε model to numerically study the basic reaction flow characteristics of the three cases. The study is conducted for an inlet temperature of 618K, FAR of 0.021, and inlet pressure of 500kPa, employing the same parameter setup of Section 4.3.

Figure 9 illustrates the axial velocity distribution of the central section of the combustion chamber for the three schemes. Figure 9 reveals that when the main and pilot stages operate simultaneously, a stable recirculation flow is generated downstream of the main and pilot stages. The shape of the recirculation area in the center section is different due to the differences in the domes. Specifically, the size of the recirculation zone downstream of the pilot stage of scheme B is the widest and longest among the three schemes.

Comparing the flow patterns of the central cross-section of the three schemes, the size of the recirculation zone formed downstream of the Venturi structure is wider and longer than that of the pure convergent structure under the same working conditions. And the main stage of the Venturi structure has a stronger influence on the shape of

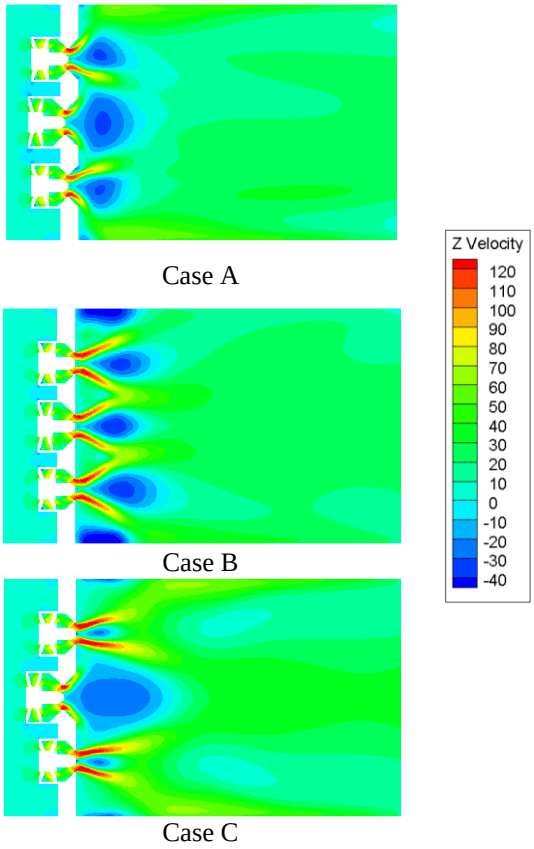

Fig. 9 Axial velocity distribution cloud map of the central section of the three cases

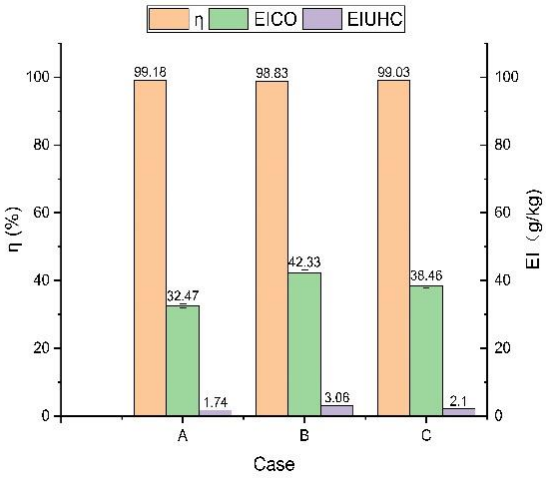

Fig. 10 Combustion efficiency at low power conditions

the downstream recirculation area of the pilot stage, limiting the development of the downstream recirculation area of the pilot stage.

5.2 Combustion Efficiency and Emissions at Low Conditions

At low conditions, two different conditions are applied to catch the combustion performances of the three cases. One condition studies the inlet temperature at 450K and pressure at 320kPa, where the pilot stage works alone, and the local equivalence ratio is rich, stabilizing the flame. The combustion efficiency, EICO, and EIUHC of the three cases are illustrated in Fig. 10.

The results highlight that the three schemes' combustion efficiency exceeds 98.5% when the pilot stage works alone. The combustion efficiency of Case A is 99.18%, the highest among the three schemes. The second is Case C, which affords a combustion efficiency of 99.03%, and the combustion efficiency of Case B is the smallest, 98.83%. This is because the swirl intensity of the Venturi cyclone is higher than the pure convergent outlet cyclone with the same swirl angle. Therefore, the recirculation zone formed by the pilot stage in Case C is larger than that in B. Moreover, the size of the primary zone is positively correlated with the recirculation zone, while the larger size of the primary zone means sufficient combustion. Therefore, the combustion efficiency of Case C is higher than B. Compared with Case A, since the main stage of Case C is a convergent outlet and its swirl intensity is weaker than A, it is easier to entrain part of the main mode swirl air into the primary zone, reducing the equivalence ratio of the primary zone. Therefore, the combustion efficiency of Case A is higher than C. In modern civil aircraft engines, the combustion efficiency should not be lower than 98.5% at low power conditions, and the three schemes studied in this paper meet this requirement.

Figure 10 infers that the outlet EICO and EIUHC of the three schemes present an opposite trend with combustion efficiency because the CO and UHC generation will decrease as the flame temperature increases.

Figure 11 illustrates the change in the pollutant emissions at the combustion chamber outlet of the three schemes. It can be seen from the figure that the NOx emission has an opposite trend to CO and UHC due to the increase of flame temperature and the NOx generated by the thermal mechanism. The research results show that Case A has the highest EINOx at the combustion chamber outlet of the three schemes, which is 1.16g/kg. This result is at a low level for advanced civil aviation engines. The EINOx at Case B and C outlets is 0.34g/kg and 0.65g/kg, respectively, 71% and 44% lower than A, both at a deficient level.

From the above results, it can be concluded that the cyclone with a pure convergent outlet can significantly reduce the NOx emissions at the combustion outlet under low working conditions when the pilot stage works alone.

Figure 12 depicts the outlet temperature distribution of the combustion chamber in the three schemes. In this paper, the total outlet temperature at 7 locations at the combustion chamber outlet is measured, and the measuring points layout is illustrated in Fig. 13, which highlights the outlet temperature distribution trend of the combustion chamber corresponding to different combustion chamber schemes is the same. All three schemes present the highest temperature at the center of the combustion chamber.

As the measuring point moves to the flame tube wall, the temperature at the combustion chamber outlet decreases because only the pilot stage works at this condition, and the high-temperature area is mainly concentrated in the primary zone. Furthermore, when the exit temperature of the combustion chamber is at section A, it is higher than the average temperature of section B. This is because only the pilot stage works at this condition, and the swirling air of the main stage will interfere with the central high-temperature zone and reduce the gas temperature downstream of the main mode cyclone.

Furthermore, Fig. 13 highlights that the outlet temperature of Scheme A is the highest, followed by Scheme C and B, which also verifies the above difference in combustion efficiency and outlet pollution emissions. Case A's average outlet temperature rise is

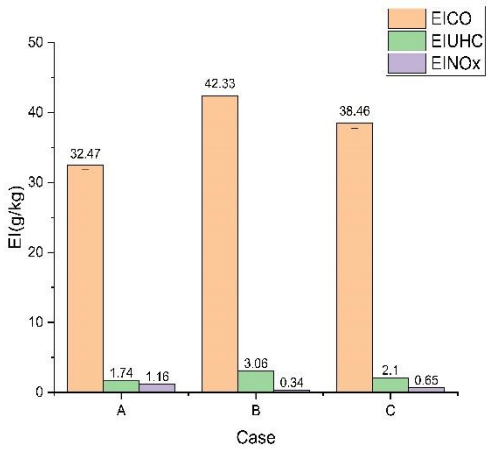

Fig. 11 Gaseous emission at low power conditions

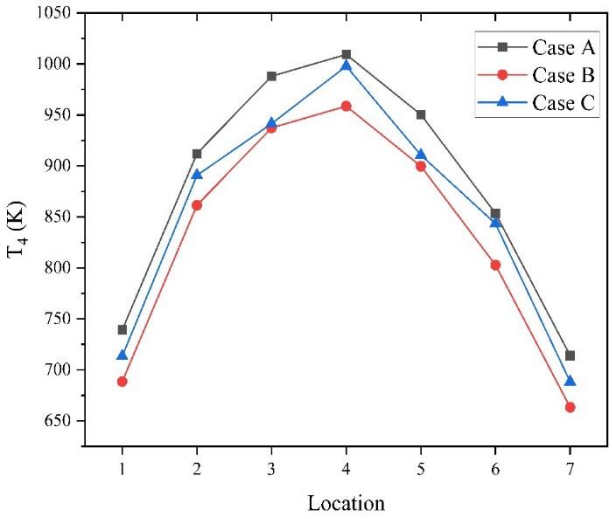

Fig. 12 T4 at low power conditions

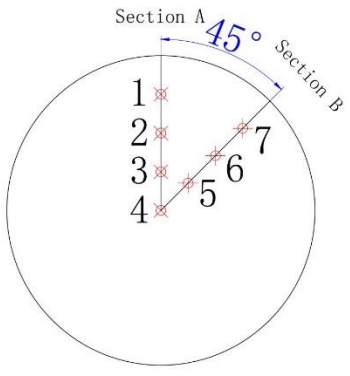

Fig. 13 measuring points of T4

greater than C, which further verifies that the main stage using the Venturi outlet structure has more potent interference with the pilot stage, affecting the pollution emission at the combustion chamber outlet.

5.3 Combustion Efficiency and Emissions at High Conditions

Given an inlet temperature of 618K, FAR of 0.021, and inlet pressure of 500kPa, we study the changes in combustion performance of the three schemes when the main and pilot stage works simultaneously.

Figure 14 illustrates the combustion efficiency, EICO, and EIUHC of the three cases at this condition, inferring that when the main and pilot stages are working simultaneously, the combustion efficiencies of the three cases exceed 99%. The combustion efficiency of scheme C is 99.75%, the highest among the three schemes, as scheme A attains 99.7% and scheme B has a combustion efficiency of 99.23%, the smallest among all schemes. This result differs from the laws of the three schemes when the pilot stage works alone. For a higher swirl intensity of the Venturi cyclone, the central recirculation zone and the recirculation zones downstream the main stage are the smallest in Case B, so the primary zone of Case B is smaller than the competitor schemes. Hence, the combustion efficiency is the lowest.

When the main and pilot stages work simultaneously, due to the heat release of the combustion reaction, the size of the main stage recirculation zone increases. At this time, the size of the center recirculation zone for Case A is affected by the interference of the main stage, which is stronger than C. In addition, due to heat release, the swirling flow of the main stage in Case A is not easy to entrain into the central recirculation zone. Therefore, compared with Case A, the size of the primary zone in Case C will be larger, and the combustion will be more thorough.

When the main and pilot stages work simultaneously, due to the heat release of the combustion reaction, the size of the main stage recirculation zone increases. At this time, the size of the center recirculation zone for Case A is affected by the interference of the main stage, which is stronger than C. In addition, due to heat release, the swirling flow of the main stage in Case A is not easy to entrain into the central recirculation zone. Therefore, compared with Case A, the size of the primary zone in Case C will be larger, and the combustion will be more thorough.

It can also be seen from the figure that the outlet EICO and EIUHC of the three schemes present an opposite trend to combustion efficiency because the CO and UHC generation decrease as the flame temperature increases.

Figure 15 shows the emissions from the combustor outlet of the three cases, revealing that the NOx emissions have an opposite trend with the CO and UHC emissions due to the increased NOx produced by the thermal mechanism because of the flame temperature increase. The results in this paper highlight that among the three cases, the EINOx of the combustion chamber in Case C is the highest at 1.86g/kg, which is already relatively low for advanced civil aviation engines. The export EINOx of Case A and B are 1.68g/kg and 1.09g/kg, respectively, reduced by 10% and 41% compared to Case C.

From the above results, it can be concluded that the cyclone with a pure convergent outlet can significantly reduce NOx emissions at the combustion outlet when the main and pilot stages work simultaneously.

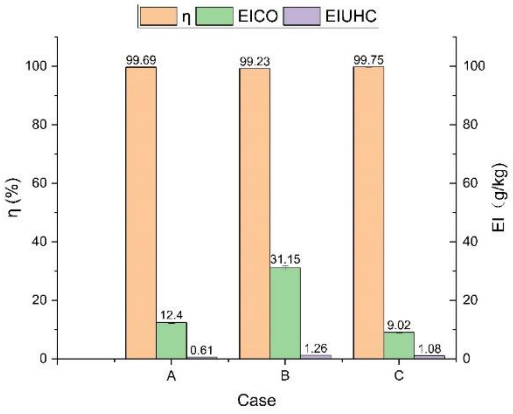

Fig. 14 Combustion efficiency at FAR=0.021

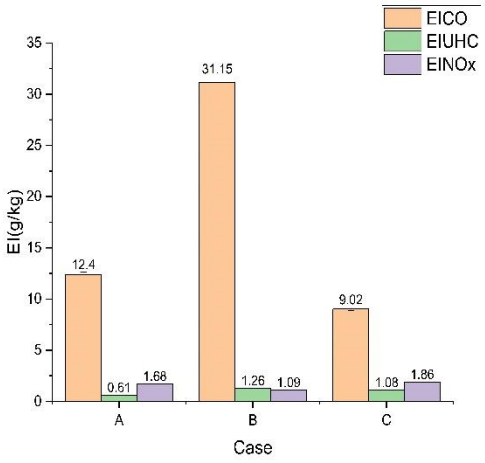

Fig. 15 Gaseous emission at FAR=0.021

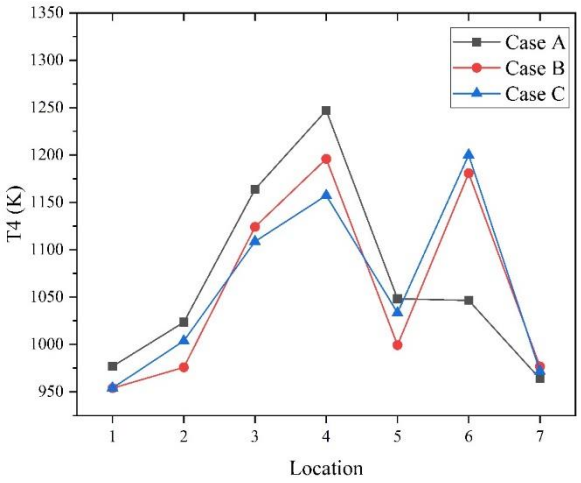

Fig. 16 T4 at FAR=0.021.

Figure 16 shows this condition's outlet temperature distribution in the three cases. Compared with the condition when the pilot stage works lonely, the outlet temperature distribution no longer presents a distribution trend of the highest center, as the lower the temperature, the closer the wall. However, the distribution trend in section B is preserved, except for the highest temperature, which is at the center of Section A. The temperature at the downstream position of the main stage also has an inevitable increase. Since the main and pilot stages work together, a stable recirculation zone is formed downstream of the main stage to produce a combustion reaction, increasing the outlet temperature downstream of the main stage. The center temperature of Case C is not the highest outlet temperature distribution, but the highest outlet temperature is located downstream of the main stage cyclone outlet. This is due to the flow and fuel distribution changes in the combustion chamber caused by different dome structures. This result also verifies that Case C's main swirl has less disturbance to the pilot, resulting in a larger size of the center recirculation zone of Case C.

5.4 The Effect of Fuel Ratio on Combustion Efficiency and Emissions

Next, we study the three combustion chamber schemes' pollutant emission and combustion performances at an inlet temperature of 700K and inlet pressure of 500kPa. Figure 17 illustrates the combustion efficiencies and outlet EICO and EIUHC emissions of the three combustion chambers under different main fuel ratios (α). Figure 17 reveals that the combustion efficiencies of the three schemes are very close and are the same for the CO and UHC emissions because the inlet temperature of the combustion chamber at this condition is relatively high. Under this condition, the change in the swirl intensity has a minor effect on the combustion performance of the combustion chamber. Under this condition, the combustion efficiencies of the three schemes exceed 99.99%. It can be further seen from the figure that as the proportion of α increases, the combustion efficiency of the three schemes remains unchanged, including the CO and UHC emissions, because the fuel can be well atomized and evaporated

and can burn completely in the combustion chamber. The change of α has little effect on combustion efficiency.

Figure 18 depicts the changes in the gas pollutant emissions of the three schemes with α, highlighting that as α increases, the outlet EINOx of the combustion chamber decrease. This is due to the increase in the ratio of main fuel, and the equivalent ratios of the main and pilot stages are getting closer, and the combustion chamber is less likely to generate local hot spots so that the outlet NOx emissions can be reduced.

The longitudinal comparison of the three schemes reveals that when α is less than 50%, the NOx emission presents Case A's lowest and B's highest emissions. When α is 60%, Case B has the lowest export NOx emission, while it is the highest for Case A because when α is lower than 50%, the stronger the swirling intensity, the larger the recirculation zone, and the larger the high-temperature zone, less likely generating hot spots localization. As α

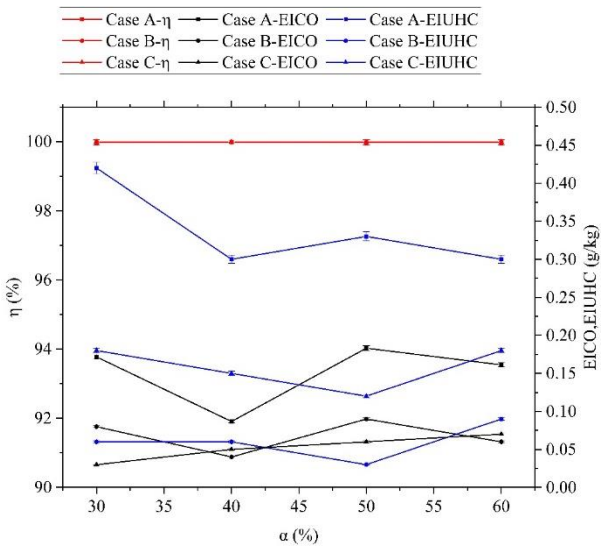

Fig. 17 Combustion efficiency at high power conditions

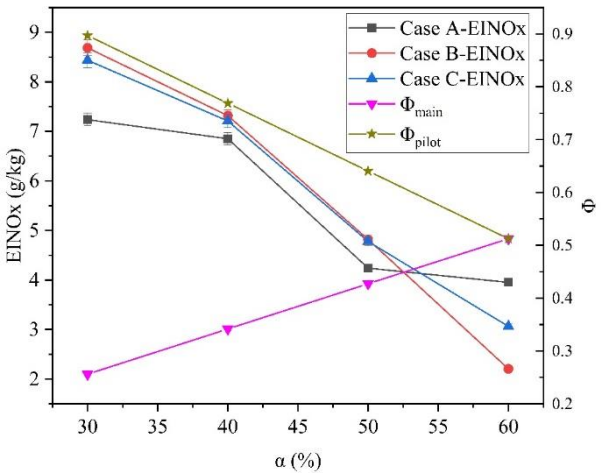

Fig. 18 Gaseous emission at high power conditions

increases, fuel and gas distribution in the combustion chamber become more uniform. At this time, a smaller recirculation zone means less gas residence time, leading to less NOx generation. Therefore, the NOx emission of the combustion chamber of the three schemes shows the law as mentioned above.

6. CONCLUSION

This paper conducts experimental research on the combustion efficiency and pollution emission characteristics of the five-point LDI combustor and obtains the following conclusions:

- When the pilot stage works alone, all three schemes have a combustion efficiency higher than 98.5%, with Case A having the highest efficiency and Case B having the lowest NOx emissions due to different swirling intensities.
- When the pilot and main stages work together, all three schemes have a combustion efficiency higher than 99.9%, with Case C having the

highest efficiency and Case B having the lowest NOx emissions due to different swirling intensities.

- NOx formation is sensitive to the α parameter, so the Φmain parameter should be close to Φpilot to reduce NOx formation.
- The cyclone with a convergent outlet has a greater advantage in reducing NOx emissions than the cyclone with a Venturi outlet.

ACKNOWLEDGEMENTS

This work supported by the National Science and Technology Major Project of China (grant numbers 2017-Ⅲ-0002-0026，J2019-Ⅲ-0012-0055，J2019-Ⅲ-0004-0047).

CONFLICT OF INTEREST

There are no conflicts to disclose.

AUTHORS CONTRIBUTION

Conceptualization, Jianqin Suo and Zhenxia Liu.; methodology, Pengfei Zhu.; validation, Pengfei Zhu, Hongxia Liang, Xiangzhou Feng and Qiandong Li.; formal analysis, Pengfei Zhu.; investigation, Pengfei Zhu; writing—original draft preparation, Pengfei Zhu; writing—review and editing, Hongxia Liang. All authors have read and agreed to the published version of the manuscript.

REFERENCES

Cai, J. (2006). Aerodynamics of lean direct injection combustor with multi-swirler arrays. (Doctoral dissertation, University of Cincinnati.). http://rave.ohiolink.edu/etdc/view?acc_num=ucin1148233034

Chen, J., Li, J., Yuan, L., & Hu, G. (2019). Flow and flame characteristics of a RP-3 fuelled high temperature rise combustor based on RQL. *Fuel*, 235, 1159-1171. https://doi.org/10.1016/j.fuel.2018.08.115

Chiming, L., Tacina, K. M., & Wey, C. (2007). High Pressure Low NOx Emissions Research: Recent Progress at NASA Glenn Research Center. https://ntrs.nasa.gov/citations/20070022362.

Davoudzadeh, F. (2004). Supersonic Rocket Thruster Flow Predicted by Numerical Simulation. https://ntrs.nasa.gov/citations/20050215166

Dewanji, D., & Rao, A. G. (2015a). Spray combustion modeling in lean direct injection combustors, Part I: Single-element LDI. *Combustion Science and Technology*, 187(4), 537-557. https://doi.org/10.1080/00102202.2014.965810

Dewanji, D., & Rao, A. G. (2015b). Spray combustion modeling in lean direct injection combustors, Part II: Multi-point LDI. *Combustion Science and Technology*, 187(4), 558-576. https://doi.org/10.1080/00102202.2014.958476

Dewanji, D., Rao, A. G., Pourquie, M. J. B. M., & Van Buijtenen, J. P. (2012). Investigation of flow characteristics in lean direct injection combustors. *Journal of Propulsion and Power*, 28(1), 181-196. https://doi.org/10.2514/1.B34264

Fan, X. J., Xu, G., Liu, C., Wang, J. , & Zhang, C. (2020) Experimental investigations of the flow field structure and interactions between sectors of a double-swirl low-emission combustor. *Journal of Thermal Science*, 29(11), 43–51. https://doi.org/10.1007/s11630-020-1228-z

Foust, M., Thomsen, D., Stickles, R., Cooper, C., & Dodds, W. (2012). Development of the GE aviation low emissions TAPS combustor for next generation aircraft engines. In 50th AIAA aerospace sciences meeting including the new horizons forum and aerospace exposition (p. 936). https://doi.org/10.2514/6.2012-936

Fristrom, R. M and Westenberg, A. A. (1965). *Flam Structure*, MeGraw-Hill.

Fu, Y. (2008). Aerodynamics and combustion of axial swirlers (Doctoral dissertation, University of Cincinnati). http://rave.ohiolink.edu/etdc/view?acc_num=ucin1204551619

Gejji, R. M., Huang, C., Yoon, C., & Anderson, W. (2014). A Parametric Study of Combustion Dynamics in a Single-Element Lean Direct Injection Gas Turbine Combustor: Part II: Experimental Investigation. In *52nd Aerospace Sciences Meeting* (p. 0133). https://doi.org/10.2514/6.2014-0133

Gugulothu, S. K. & Nutakki, P. K. (2019). Dynamic fluid flow characteristics in the hydrogen-fuelled scramjet combustor with transverse fuel injection. *Case Studies in Thermal Engineering*, 14, 100448. https://doi.org/10.1016/j.csite.2019.100448

Hatem, F. A., Alsaegh, A. S., Al-Faham, M., Valera-Medina, A., Chong, C. T., & Hassoni, S. M. (2018). Enhancing flame flashback resistance against Combustion Induced Vortex Breakdown and Boundary Layer Flashback in swirl burners. *Applied energy*, 230, 946-959. https://doi.org/10.1016/j.apenergy.2018.09.055

Heath, C. M. (2014). Characterization of swirl-venturi lean direct injection designs for aviation gas turbine combustion. *Journal of Propulsion and Power*, 30(5), 1334-1356. https://doi.org/10.2514/1.B35077

Heath, C. M. (2016). Parametric modeling investigation for radially staged low-emission combustion. *Journal of Propulsion and Power*, 32(2), 500-515. https://arc.aiaa.org/doi/10.2514/1.B35867

Hicks, Y. R. & Tacina, M. (2013, July). Comparing a Fischer-Tropsch Alternate Fuel to JP-8 and their 50-50 Blend: Flow and Flame Visualization Results. In *2012 Central States Section of the Combustion*

Institute Spring Technical Meeting (No. NASA/TM-2013-217884). https://ntrs.nasa.gov/citations/20140000730

Hicks, Y. R., Heath, C. M., Anderson, R. C., & Tacina, K. M. (2012, April). Investigations of a combustor using a 9-point swirl-venturi fuel injector: recent experimental results. In *20th International Symposium on Air Breathing Engines (ISABE 2011)* (No. E-18001). https://ntrs.nasa.gov/citations/20120008517

Huang, C., Gejji, R. M., Anderson, W. E., Yoon, C., & Sankaran, V. (2014). Combustion dynamics behavior in a single-element lean direct injection (ldi) gas turbine combustor. In *50th AIAA/ASME/SAE/ASEE Joint Propulsion Conference* (p. 3433). https://doi.org/10.2514/6.2014-3433

Huang, C., Gejji, R., Anderson, W., Yoon, C., & Sankaran, V. (2020). Combustion dynamics in a single-element lean direct injection gas turbine combustor. *Combustion Science and Technology*, 192(12), 2371-2398. https://doi.org/10.1080/00102202.2019.1646732

Kyprianidis, K. G. & Dahlquist, E. (2017). On the trade-off between aviation NOx and energy efficiency. *Applied Energy*, 185, 1506-1516. https://doi.org/10.1016/j.apenergy.2015.12.055

Li, Y., Jia, Y., Jin, M., Zhu, X., Ge, B., Mao, R., Ren, L., Chen, M., & Jiao, G. (2022). Experimental Investigations on NO x Emission and Combustion Dynamics in an Axial Fuel Staging Combustor. *Journal of Thermal Science*, 31, 198-206. https://doi.org/10.1007/s11630-022-1562-4

Lieuwen, T. C. & Yang, V. (Eds.). (2013). Gas turbine emissions (Vol. 38). Cambridge university press. https://lccn.loc.gov/2012051616

Lieuwen, T., Torres, H., Johnson, C., & Zinn, B. T. (2001). A mechanism of combustion instability in lean premixed gas turbine combustors. *Journal of Engineering for Gas Turbines and Power*, 123(1), 182-189. https://doi.org/10.1115/1.1339002

Mckinney, R. Cheung, A., Sowa, W., & Sepulveda, D. (2007, January). The Pratt & Whitney TALON X low emissions combustor: revolutionary results with evolutionary technology. In *45th AIAA aerospace sciences meeting and exhibit* (p. 386). https://doi.org/10.2514/6.2007-386

Mongia, H. (2003). TAPS: A fourth generation propulsion combustor technology for low emissions. In AIAA International Air and Space Symposium and Exposition: The Next 100 Years (p. 2657). https://doi.org/10.2514/6.2003-2657

Patel, N., & Menon, S. (2008). Simulation of spray–turbulence–flame interactions in a lean direct injection combustor. *Combustion and Flame*, 153(1-2), 228-257. https://doi.org/10.1016/j.combustflame.2007.09.011

Patel, N., Kırtaş, M., Sankaran, V., & Menon, S. (2007). Simulation of spray combustion in a lean-direct injection combustor. *Proceedings of the Combustion Institute*, 31(2), 2327-2334. https://doi.org/10.1016/j.proci.2006.07.232

Raju, M. S., & Wey, C. T. (2020). CFD Predictions of Soot & CO Emissions Generated by a Partially-Fueled 9-Element Lean-Direct Injection Combustor. In *AIAA Scitech 2020 Forum* (p. 2088). https://doi.org/10.2514/6.2020-2088

SAE International (2011). Procedure for the continuous sampling and measurement of non-volatile particle emissions from aircraft turbine engines. https://infostore.saiglobal.com/en-us/standards/sae-arp-1256-2011-1018428_saig_sae_sae_2370568/

SAE International (2013). Procedure for the Analysis and Evaluation of Gaseous Emissions from Aircraft Engines. https://infostore.saiglobal.com/en-us/standards/sae-arp-1533-2013-1022736_saig_sae_sae_2382526/

Tacina, K. M., & Wey, C. (2008). NASA Glenn high pressure low NOx emissions research (No. E-16137). https://ntrs.nasa.gov/citations/20080014197

Tacina, K. M., Lee, P., Mongia, H., Dam, B. K., He, Z. J., & Podboy, D. P. (2016). A comparison of three second-generation swirl-venturi lean direct injection combustor concepts. In *52nd AIAA/SAE/ASEE Joint Propulsion Conference* (p. 4891). https://doi.org/10.2514/6.2016-4891

Tedder, S. A., Tacina, K. M., Anderson, R. C., & Hicks, Y. R. (2014). Fundamental study of a single point lean direct injector. Part I: effect of air swirler angle and injector tip location on spray characteristics. In *50th AIAA/ASME/SAE/ASEE Joint Propulsion Conference* (p. 3435). https://doi.org/10.2514/6.2014-3435

Tian, L., Sun, H., Xu, Y., Jiang, P., Lu, H., & Hu, X. (2022). Numerical analysis on combustion flow characteristics of jet-stabilized combustor with different geometry. *Case Studies in Thermal Engineering*, 32, 101885. https://doi.org/10.1016/j.csite.2022.101885

Wang, B., Zhang, C., Lin, Y., Hui, X., & Li, J. (2017). Influence of main swirler vane angle on the ignition performance of TeLESS-II combustor. *Journal of Engineering for Gas Turbines and Power*, 139(1), 011501. https://doi.org/10.1115/1.4034154

Wang, K., Fan, X., Liu, F., Liu, C., Lu, H., & Xu, G. (2021). Experimental studies on fuel spray characteristics of pressure-swirl atomizer and air-blast atomizer. *Journal of Thermal Science*, 30, 729-741. https://doi.org/10.1007/s11630-021-1320-z

Wang, Y., Wu, J., & Lin, Y. (2020). Effects of confinement length of the central toroidal recirculation zone partly confined by the small pilot stage chamber on ignition characteristics. *Aerospace Science and Technology*, 107, 106277. https://doi.org/10.1016/j.ast.2020.106277

Xi, Z., Liu, Z., Shi, X., Lian, T., Li, Y. (2022). Numerical

investigation on flow characteristics and emissions under varying swirler vane angle in a lean premixed combustor, *Case Studies in Thermal Engineering*, 31, 101800. https://doi.org/10.1016/j.csite.2022.101800

Xu, Q., Shen, M., Shi, K., Liu, Z., Feng, J., Xiong, Y., ... & Du, Y. (2021). Influence of jet angle on diffusion combustion characteristics and NOx emissions in a self-reflux burner. Case Studies in Thermal Engineering, 25, 100953. https://doi.org/10.1016/j.csite.2021.100953

Yu, H., Suo, J., Liang, H., & Zheng, L. (2016). Experimental Study on Effusion Cooling with Tangential Air Inlet. *In 52nd AIAA/SAE/ASEE Joint Propulsion Conference* (p. 5053). https://doi.org/10.2514/6.2016-5053

Zargar, O. A. (2020). Improving combustion performance of swirling double-concentric jets flames with rich equivalence ratios. *Case Studies in Thermal Engineering*, 20, 100648. https://doi.org/10.1016/j.csite.2020.100648

Zhu Z, Xiong Y, Zheng X, Chen, W., Ren, B., & Xiao, Y. (2021). Experimental and numerical study of the effect of fuel/air mixing modes on NO x and CO Emissions of MILD combustion in a boiler burner. Journal of Thermal Science, 30, 656-667. https://doi.org/10.1007/s11630-020-1323-1

APPENDIX

MEASUREMENT UNCERTAINTY ANALYSIS

The uncertainty analysis method is given in the SAE ARP 1533 (SAE, 2013). For the dependent variable y=f (x1, x2, …xn), the uncertainty in y due to the xi is shown in Eq.(A1).

$$\left(\frac{\Delta y}{y}\right)^2 = \sum_i \left(\frac{\partial lny}{\partial lnx_i}\right)^2 \left(\frac{\Delta x_i}{x_i}\right)^2 \tag{A1}$$

The emission indices and efficiency equations are shown in Eq.(A2-A5).

$$\mathrm{EICO} = \left(\frac{[\mathrm{CO}]}{\mathrm{sum}}\right)\left(\frac{10^3 \cdot \mathrm{M_{co}}}{\mathrm{M_c}+\alpha \mathrm{M_H}}\right)\left(1+\frac{\mathrm{TX}}{\mathrm{m}}\right) \tag{A2}$$

$$\mathrm{EINOx} = \left(\frac{[\mathrm{NOx}]}{\mathrm{sum}}\right)\left(\frac{10^3 \cdot \mathrm{M_{NOx}}}{\mathrm{M_c}+\alpha \mathrm{M_H}}\right)\left(1+\frac{\mathrm{TX}}{\mathrm{m}}\right) \tag{A3}$$

$$\mathrm{EIUHC} = \left(\frac{[\mathrm{UHC}]}{\mathrm{sum}}\right)\left(\frac{10^3 \cdot \mathrm{M_{UHC}}}{\mathrm{M_c}+\alpha \mathrm{M_H}}\right)\left(1+\frac{\mathrm{TX}}{\mathrm{m}}\right) \tag{A4}$$

$$\eta = \left(1.00 - 4.346 \cdot \frac{\mathrm{EICO}}{\mathrm{H_c}} - \frac{\mathrm{EIUHC}}{1000}\right) \cdot 100 \tag{A5}$$

The values and definitions of the parameters in the above equations can be found in the SAE ARP 1533 (SAE, 2013). Furthermore, the measurement uncertainty of each test data could be obtained by solving Eq. (A1-A5), where the accuracy of each analyzer is presented in Table.3.